

Cell-Membrane-Coated Synthetic Nanomotors for Effective Biodetoxification

Zhiguang Wu, Tianlong Li, Wei Gao, Tailin Xu, Beatriz Jurado-Sánchez, Jinxing Li, Weiwei Gao, Qiang He, Liangfang Zhang,* and Joseph Wang*

A red blood cell membrane-camouflaged nanowire that can serve as new generation of biomimetic motor sponge is described. The biomimetic motor sponge is constructed by the fusion of biocompatible gold nanowire motors and RBC nanovesicles. The motor sponge possesses a high coverage of RBC vesicles, which remain totally functional due to its exclusively oriented extracellular functional portion on the surfaces of motor sponge. These biomimetic motors display efficient acoustical propulsion, including controlled movement in undiluted whole blood. The RBC vesicles on the motor sponge remain highly stable during the propulsion process, conferring thus the ability to absorb membrane-damaging toxins and allowing the motor sponge to be used as efficient toxin decoys. The efficient propulsion of the motor sponges under an ultrasound field results in accelerated neutralization of the membrane-damaging toxins. Such motor sponges connect artificial nanomotors with biological entities and hold great promise for treating a variety of injuries and diseases caused by membrane-damaging toxins.

1. Introduction

Inspired by the motor-like properties of a myriad of biomolecules and organisms, considerable efforts have been devoted to the development of artificial nanomotors powered by different propulsion mechanisms owing to their great promise for diverse applications.^[1–15] To better mimic the functions of natural motors, recent efforts have shifted to modifying artificial nanomotors with biological entities, particularly bioreceptors, toward more versatile and robust biomedical and sensing applications.^[16–19] As a result, various types of biomolecules such as enzymes, antibodies, nucleic acids, lectins, and aptamers have been utilized to functionalize nanomotors for performing demanding tasks ranging from bioisolation to targeted drug delivery.^[20–23] While effective in performing certain tasks, the strategy of integrating a single type of biological molecules onto

synthetic nanomotors is largely insufficient to achieve complex functions that natural organisms possess. Therefore, more advanced biomimetic motors are highly desirable but remain elusive to materials and biomedical researchers. An ideal biomimetic nanomotor is expected to operate effectively in biological environment over extended periods to accomplish comprehensive biological tasks.

As a long-circulating delivery vehicle in nature, red blood cells (RBCs) possess attractive biological properties and continue to inspire the design and engineering of various types of man-made biomimetic delivery systems.^[24–26] The pursuit of RBC-mimicking nanostructures has recently led to the development of an intriguing approach of functionalizing synthetic nanoparticles with natural RBC membranes.^[27] In this approach, cellular

membranes are directly collected from RBCs and then coated onto polymeric nanoparticle cores, resulting in RBC membrane-coated nanoparticles. These biomimetic nanoparticles have shown unprecedented capability to harness natural functionalities of the native cells that would otherwise be difficult to replicate, including evading the immune system for prolonged circulation in the bloodstream. More interestingly, such RBC membrane-coated particles have also shown excellent capability to function as a toxin nanosponge to cleanse the body of various virulence factors such as those caused by bacterial infections, venomous injuries, and biological weaponry.^[28–30] While considerable progress has been made on using natural RBC membranes to coat and thus camouflage inert synthetic nanoparticles for biomedical uses,^[31–35] there are no reports coupling such cell membrane coating technology with powered nanomotors to create biomimetic motors for more dynamic and versatile applications.

This article reports the development and characterization of a biomimetic nanomotor prepared by fusing ultrasmall RBC membrane-derived vesicles onto the surface of an ultrasound-propelled artificial gold nanowire motor. The high surface tension of RBC vesicles and their electrostatic repulsion with the citrate-modified gold nanowires result in effective fusion and coverage of RBC vesicles onto the nanowires with a right-side-out orientation, similar to what has been observed on the RBC membrane-coated polymeric nanoparticle system.^[36] Bridging such groundbreaking RBC-based sponges and state-of-the-art fuel-free artificial nanomotors results in a powerful biomimetic

Z. Wu, T. Li, Dr. W. Gao, T. Xu, Dr. B. Jurado-Sánchez, J. Li, Dr. W. Gao, Prof. L. Zhang, Prof. J. Wang
Department of Nanoengineering
University of California
San Diego, La Jolla, CA 92093, USA
E-mail: zhang@ucsd.edu; josephwang@ucsd.edu

Z. Wu, T. Li, Prof. Q. He
Micro/Nanotechnology Research Center
Harbin Institute of Technology
Harbin 150080, China



DOI: 10.1002/adfm.201501050

platform for diverse applications. Owing to the unique RBC membrane coating, these biomimetic nanomotors represent the first example of synthetic motors that act as decoys to attract and absorb “on-the-fly” different types of membrane-damaging toxins and offer remarkable biocompatibility and propulsion in various biological fluids. Significantly, imparting dynamic movement onto nanosponges greatly enhances the toxin–sponge interactions and dramatically accelerates their toxin neutralization ability, compared to regular toxin sponges whose mobility is solely relying on Brownian motion. Such biomimetic nanomotors represent a new class of hybrid motors, which combine the attractive properties of synthetic nanomotors with those of biological membranes. These cell-membrane camouflaged nanowire motors are expected to open the door to the design and development of bioinspired motors with robust functionalities and diverse applications.

2. Results and Discussion

Figure 1A illustrates the fabrication process of the RBC membrane-coated gold nanomotors (denoted “motor sponges”), consisting of the preparation of gold nanowires and coating with a functional layer of RBC membranes. The bare gold nanomotors were fabricated through a common membrane template electrodeposition protocol.^[37] Such template-assisted method enables a rapid large-scale production of gold nanowires having concave structure on one end (corresponding to the growth side), instead of a flat one, as required for efficient acoustic energy harvesting and propulsion.^[37] Further details of the preparation process can be found in the Supporting Information. The resulting bare nanomotors undergo an ex situ stabilization (which will also play an important role in the incorporation of the RBC membranes) by incubating overnight with citric acid to introduce negative charge onto the gold surface.^[38,39] The negatively charged gold nanomotors were subsequently incubated with RBC membrane-derived vesicles (diameter 50–100 nm) under ultrasonication. The small RBC vesicles with high surface tension were not stable and prone to fuse onto the solid gold surface to minimize the free energy of the system. The ultrasonic agitation enhanced the absorption of RBC vesicles onto the gold nanomotors. The fusion process retained the inherent bilayer structure of the RBC membrane and preserved the function of the membrane proteins. More

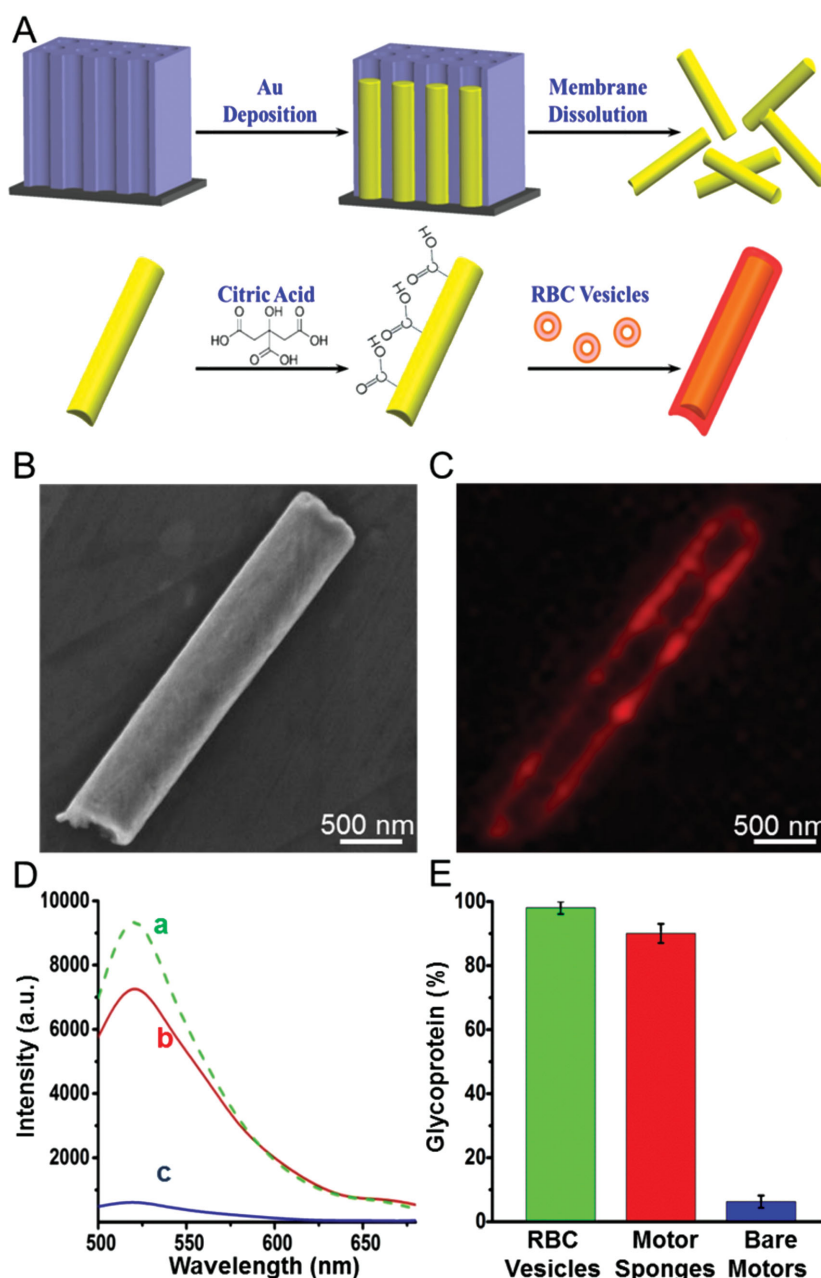


Figure 1. Synthesis and characterization of RBC membrane-coated gold nanomotors (denoted “motor sponges”). A) Schematic preparation of motor sponges consisting of an ultrasound-propelled gold nanowire motor coated with RBC membranes. B) Scanning electron microscope (SEM) image of a fabricated motor sponge. C) Fluorescent image of a motor sponge, of which the RBC membranes were stained with Rhodamine B. D) Determination of the membrane coverage on the motor sponges using a fluorescence quenching assay. Fluorescence spectra of a) FITC-thiol alone, b) FITC-thiol and motor sponge mixture, and c) FITC-thiol and bare motor mixture. (E) Evaluation of the orientation of RBC membranes on the motors by comparing the relative glycoprotein content of the RBC vesicles, motor sponges, and bare motors.

importantly, due to the asymmetric negative charge between the exoplasmic and cytoplasmic sides of RBC membranes, the outer surface of the RBC membrane is much more negatively charged than the inner surface. Therefore, the fusion of RBC vesicles onto the negatively charged motors resulted in a

right-side-out orientation of the membranes due to electrostatic repulsion.^[40] In this case, the resulting motor sponges carried the functional proteins on the extracellular surfaces of RBCs.

Figure 1B shows the scanning electron microscope (SEM) image of a motor sponge (400 nm in diameter and 3 μm in length) with a concave on one end. This image indicates that the characteristic nanowire shape of the motor, with its concave end, is not affected by the RBC coating, as expected from the 6–8 nm thick fluid-like lipid bilayer, compared to the 400 nm diameter gold motors. The template deposition method, used in the presence work, ensures such formation of a concave structure on one end of the gold nanowire.^[37,41] To confirm the presence of RBC membranes on the motor surface, Rhodamine B (RhB) stained RBC vesicles were fused with the nanomotors. The fluorescent image in Figure 1C illustrates the full coverage of the motor sponge, indicating the successful incorporation of RhB-stained RBC vesicles onto the citrate-stabilized nanomotors. The coverage of RBC membranes on the surface of motor sponges was also evaluated using the interaction of the motor sponges with a thiolated fluorescent ligand.^[31] A fluorescein isothiocyanate (FITC)–thiol conjugate probe was synthesized by conjugating FITC to cysteamine 4-methoxytrityl through *N*-hydroxysuccinimide (NHS)-mediated amine coupling, and subsequently cleaning the conjugate from the resin using trifluoroacetic acid. The FITC–thiol strongly binds to the uncoated surface of gold nanomotor owing to gold–thiol interaction, after which the gold nanomotor can quench the fluorescence emission of FITC in a distance-dependent manner. In contrast, when the gold surface is covered by RBC membranes, the FITC–thiol will not bind. Therefore, the coverage of RBC membranes can be determined by measuring the quenching effect of FITC–thiol by the gold motor. Figure 1D shows the

fluorescence emission spectra of free FITC–thiol, FITC–thiol with motor sponges, and FITC–thiol with bare motors (without RBC membrane coating). Compared to free FITC–thiol, the greatly reduced fluorescence intensity of FITC–thiol incubated with bare motors at its emission peak of 520 nm reflects the effect of fluorescence quenching. In contrast, the quenching effect is not obvious when FITC–thiol was incubated with the motor sponges. The results clearly indicate the high coverage of RBC membranes on the surface of gold nanomotors that shield the binding between the nanomotors and the FITC–thiol.

Most functionalities of RBCs, including immune evasion and toxin-binding abilities, rely on the right orientation (right-side-out) of the RBC membrane. This is because the membrane itself is highly asymmetric. Its two (outside and inside) surfaces differ significantly in their membrane composition and distribution. Therefore, it is critical to ensure that the membrane coated on the nanomotor adapts a right-side-out function orientation. Subsequently, we assessed the orientation of RBC membranes in a right-side-out manner on the motor sponge surface by the quantification of glycoprotein on the RBC membranes, which exclusively distributed on the extracellular side of the membranes. To this end, trypsin was first incubated with motor sponges to cleave the glycoprotein from the RBC membranes. Considering the impermeability of trypsin to the RBC membranes on the motor sponges, the enzymatically removed glycoprotein can be used to assess the membrane sidedness. The content of detached glycoprotein was quantified using a periodate-based glycoprotein detection assay following a published protocol.^[36] As shown in Figure 1E, the glycoprotein content of motor sponges is near 90% to the equivalent amount of free RBC vesicles. This suggests that the majority of the glycoproteins on the motor sponges present on the outer

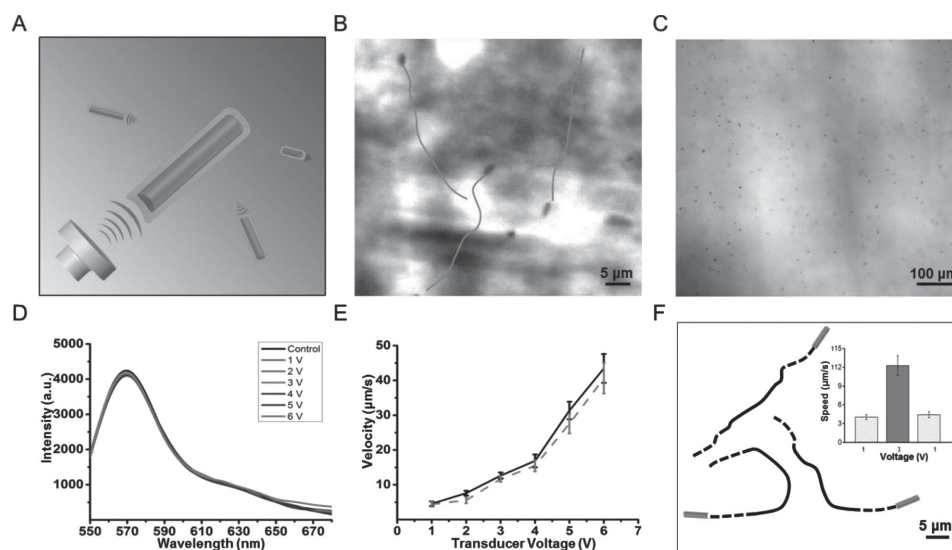


Figure 2. Ultrasound propulsion of motor sponges. A) Schematic illustration of ultrasound-propelled motor sponges. B) Time-lapse images (taken from Video 1, Supporting Information) illustrating random motion and moving distances of three motor sponges in deionized water with a transducer voltage of 5 V and a frequency of 2.83 MHz. C) A large population of moving motor sponges under the ultrasound field. D) Fluorescence spectra illustrating the stability of RBC membrane coating on the motor sponges under ultrasound fields with transducer voltage over the range 0–6 V. E) Dependence of the average speed of motor sponges (dash line) and bare motors (solid line) upon the ultrasound voltage. F) Speed modulation of ultrasound-propelled motor sponges in response to a low/high/low (1/3/1 V) 6 s potential steps using a frequency of 2.83 MHz. Dash and solid track lines showing the motor trajectories at applied potentials of 1 and 3 V, respectively.

surface, which corresponds to a right-side-out orientation of the RBC membrane on the motor sponges. Such orientation of RBC membrane facilitates the selective uptake of pore-forming toxins and protects the motor sponge from the nonspecific adsorption of proteins (biofouling) in biological media, i.e., the biomimetic motor acting as a decoy of natural RBCs.

The presence of the concave end, obtained by the template deposition, ensures efficient motion triggered by the external ultrasound field. Such fast acoustic propulsion of the nanowire motor sponges within the levitation plane derives from acoustically driven fluid streaming around their axially asymmetric concave ends that lead to efficient energy harvesting (Figure 2A).^[41–44] The trajectories in the time-lapse image of Figure 2B, taken from Video 1 in the Supporting Information, illustrate the travel distance of three motor sponges with an average speed of $32 \mu\text{m s}^{-1}$ over a 1 s period in distilled water using an ultrasound frequency of 2.83 MHz and transducer voltage of 5 V. Application of the acoustic field results in a planar standing wave that leads to the formation of nodes and antinodes and results in pressure gradients, which drive the nanomotors toward low-pressure regions due to the primary radiation force from acoustic field.^[42,44] These motor sponges display a rapid random motion in the node plane, characteristic of ultrasound-powered movement of metallic nanowire motors.^[41] In addition, an effective population of efficiently propelled motor sponges is observed using a high concentration of motor sponges under similar ultrasound conditions (Figure 2C). Such efficient propulsion and fluid stream toward the pressure node result in a greatly improved fluid transport.

To evaluate the stability of the motor sponges, RhB-stained RBC vesicles were employed to prepare fluorescently labeled motor sponges. Figure 2D illustrates the fluorescence intensities of the RhB-labeled motor sponges during 1 h acoustic propulsion under different ultrasound transducer voltages ranging from 1 to 6 V. The negligible change of the fluorescence intensity during this operation reflects the remarkably high stability of RBC membranes on the gold motor surface. The influence of the RBC membrane coating on the propulsion performance of motor sponges was also investigated. Figure 2E shows the dependence of the speed of motor sponges and bare motors upon the ultrasound transducer voltage. The average speed of bare motors increases from $5 \mu\text{m s}^{-1}$ at 1 V to $43 \mu\text{m s}^{-1}$ at 6 V. The motor sponges exhibit a similar trend, with slightly lower speeds ranging from 4 to $41 \mu\text{m s}^{-1}$ over the same 1–6 V range. These data imply that the coverage of RBC membranes has a minimal effect on the propulsion behavior of the motor sponges. Such dependence on the ultrasound transducer potential can be exploited for real-time speed modulation of the

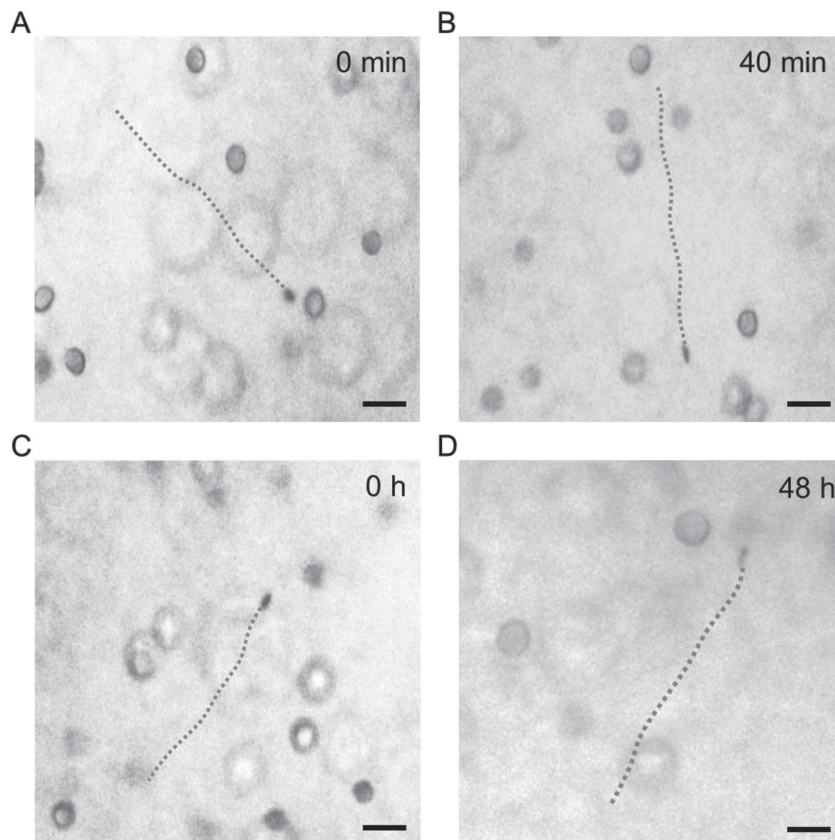


Figure 3. Propulsion of motor sponges in whole blood. A,B) Time-lapse images showing the propulsion of motor sponges in the whole blood over 40 min. C,D) Time lapse images (taken from Video 4, Supporting Information) showing the propulsion of motor sponges in whole blood before and after 48 h incubation in the whole blood, respectively. Scale bars, 10 μm . Ultrasound field conditions: 5 V and 2.83 MHz.

motor sponges. For example, Figure 2F (taken from Video 3, Supporting Information) illustrates the on-demand acceleration or deceleration of motor sponges by modulating the transducer potential. The speed of the motor sponges increases rapidly from 4 to $13 \mu\text{m s}^{-1}$ upon increasing the voltage from 1 to 3 V, and decreases rapidly back to $4 \mu\text{m s}^{-1}$ upon decreasing the voltage to 1 V again. Such precise and rapid speed control holds promise for a variety of practical applications of the motor sponges.

Since the motor sponges are covered by natural RBC membranes, they are expected to be biocompatible in whole blood and unaffected by blood-induced biofouling effects that may hinder their movement. Such biomimetic nanomotors are thus expected to operate effectively in biological environment over extended periods. The time-lapse images in Figure 3 and the corresponding Videos 4 and 5 (Supporting Information) illustrate the movement of motor sponges in undiluted whole blood using an ultrasound voltage of 5 V and a frequency of 2.83 MHz. Efficient propulsion at a speed of $14 \mu\text{m s}^{-1}$ is observed. As compared to the $27 \mu\text{m s}^{-1}$ speed in distilled water, the lower speed in whole blood reflects the high viscosity of the blood medium, as was reported for other ultrasound motors.^[37] The motor sponge displays a long-term efficient ultrasound propulsion in whole blood. The time-lapse images in Figure 3A,B,

taken from Video 4 (Supporting Information), show the ultrasound-powered propulsion of motor sponges in the whole blood at 0 and 40 min, respectively. No change in the speed of the motors is observed over this prolonged operation in the blood medium ($14 \mu\text{m s}^{-1}$ in 0 min, and $14 \mu\text{m s}^{-1}$ in 40 min). To further investigate the antibiofouling of the motor sponges in whole blood, the motors were incubated in undiluted blood for 48 h prior to monitoring their propulsion. The time-lapse images of Figure 3C,D, taken from Video 5 (Supporting Information), illustrate the ultrasound-powered movement of motor sponges before and after the 48 h incubation in whole blood, respectively. The motor sponges display efficient propulsion, with similar speeds before and after the incubation, indicating that the prolonged incubation in whole blood has negligible impact upon their propulsion behavior and that fouling effects are negligible. Similarly, Video 6 (Supporting Information) displays the efficient propulsion of multiple nanomotors in whole blood. Comparing the ultrasound-powered movement of motor sponges and bare motors in whole blood (shown in Figure S1 and Video 6, Supporting Information) further demonstrates the blood-induced biofouling and greatly hindered movement of the bare motors, compared to the absence of fouling effects using the motor sponges.

After having characterized the preparation and properties of the motor sponges, we next tested their application as a powered toxin nanosponge to effectively absorb and neutralize pore-forming toxins—a family of toxins that target RBCs by punching holes to the cell membranes. As illustrated in Figure 4A, the

large-scale collective motion can greatly enhance the interaction between the toxins and the motor sponges, thereby accelerating the toxin neutralization process as compared to the regular toxin sponges without motor functions. To investigate such neutralization action of the motor sponges, melittin (a membrane pore-forming peptide from bee venom) was employed as a model membrane-damaging toxin. By wrapping RBC vesicles on the surface of the nanomotors, the sponge nanomotors can serve as a decoy to attract toxins and thus divert the toxins away from natural cells. Experiments were performed by mixing fixed amounts of the toxin with equivalent amounts of phosphate buffered saline (PBS) buffer, bare motors (without RBC coating), motor sponges without ultrasound propulsion, or motor sponges with ultrasound propulsion for 2 min. Subsequently, the four formulations were added to 1.6 mL of 1 vol% purified mouse RBCs in PBS, respectively. Comparison of the different treatments, shown in Figure 4B, illustrates that the motor sponges are capable of protecting RBCs from lysing by melittin, and the propulsion of the motor sponges further enhanced the clean efficiency of melittin. To further confirm these observations, the relative hemolysis was quantified by measuring the absorption of the released hemoglobin at 540 nm. Figure 4C shows the percentage of hemolysis of the different treatments as a function of time. In samples treated with PBS buffer or bare motors, the relative hemolysis increases considerably to 71% within the first 10 min, and more slowly to 78% in the subsequent 30 min. In contrast, in samples treated with motor sponges under the ultrasound field, the increase in

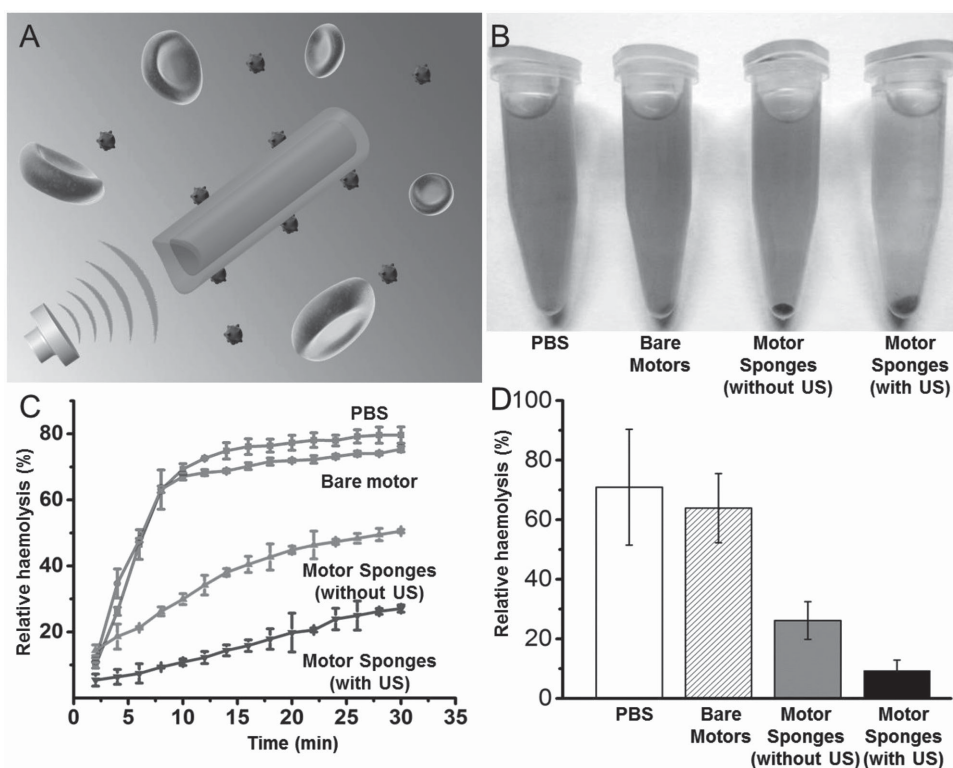


Figure 4. In vitro neutralization of pore-forming toxins by motor sponges. A) Schematic mechanism for the neutralization of mellitin toxin using ultrasound-propelled motor sponges. B) Centrifuged RBCs after incubation with melittin mixed in PBS, bare motors, motor sponges without ultrasound propulsion, and motor sponges with ultrasound propulsion. C) Hemolysis analysis of samples in (B) as the function of time (0–30 min). D) Percentage of hemolysis of samples in (B) after 10 min incubation. Ultrasound field conditions: 5 V and 2.83 MHz.

relative hemolysis is less than 20% within 30 min. During the same time window, motor sponges without ultrasound field led to relative hemolysis of about 50%. Figure 4D shows the quantitative hemolysis of the four samples after 10 min of incubation with RBCs and melittin. These results clearly demonstrate the advantage of using ultrasound-propelled motor sponges to absorb and neutralize toxins, which are about 60% more effective than PBS and bare motors and about 30% better than regular motor sponges without the ultrasound field. Apparently, imparting fast movement onto nanosponges results in a dramatically accelerated neutralization of membrane-damaging toxins, as compared to regular nanosponges that rely solely on Brownian motion. Such motion-based accelerated neutralization reflects the greatly increased fluid transport and enhanced likelihood of toxin contact with the moving sponge.

3. Conclusions

We described the first example of RBC membrane-coated artificial nanomotors, namely motor sponges, which combine the attractive properties of synthetic nanomotors and natural cell membranes toward efficient movement in body fluids and rapid neutralization of membrane-damaging toxins. The synergy of combining the nanosponges with artificial nanomotors leads to powerful platform for various biomedical applications. This new class of biomimetic nanomotors is prepared by fusing small RBC membrane-derived vesicles onto the surface of ultrasound-powered gold nanowire motors, thus displaying remarkable biocompatibility in biological fluids. The concave end of the motor sponges allows for high speed propulsion and precise directional control. Coated by natural RBC membranes, these ultrasound-propelled motor sponges can effectively and rapidly remove membrane-damaging toxins from biological fluids through a combination of toxin absorption and enhanced fluid transport. The development of the ultrasound-propelled motor sponges represents a novel biomimetic generation of synthetic motors that bridges the longstanding gap between synthetic motors and biological systems. If needed, membranes from other types of cells, such as cancer cells and stem cells, can also be employed to prepare cancer-targeting motor sponges.^[45] These cell-membrane camouflaged nanowire motors represent a new class of small-scale motors that hold great potential for a wide range of practical biomedical and biodefense applications.

Supporting Information

Supporting Information is available from the Wiley Online Library or from the author.

Acknowledgements

Z.W., T.L., and W.G. contributed equally to this work. This project was supported by the Defense Threat Reduction Agency Joint Science and Technology Office for Chemical and Biological Defense (Grant Nos. HDTRA1-13-1-0002 and HDTRA1-14-1-0064). Z.W., T.L., and T.X. were supported by the Scholarship Fund from China Scholarship Council

(CSC). B.J.-S. acknowledges support from the EU 7th Framework Programme under REA Grant PIOF-GA-2012-326476. The authors greatly thank Fei Wang for providing the RBC vesicles. The authors also thank Dr. Che-Ming J. Hu, Brian T. Luk, and Dr. Soracha Thamphiwatana for helpful discussions.

Received: March 17, 2015

Revised: April 17, 2015

Published online:

- [1] J. Wang, *Nanomachines: Fundamentals and Applications*, Wiley, New York 2013.
- [2] W. F. Paxton, K. C. Kistler, C. C. Olmeda, A. Sen, S. K. St. Angelo, Y. Cao, T. E. Mallouk, P. E. Lammert, V. H. Crespi, *J. Am. Chem. Soc.* **2004**, *126*, 13424.
- [3] W. Wang, W. Duan, S. Ahmed, T. E. Mallouk, A. Sen, *Nano Today* **2013**, *8*, 531.
- [4] Y. Mei, A. A. Solovov, S. Sanchez, O. G. Schmidt, *Chem. Soc. Rev.* **2011**, *40*, 2109.
- [5] J. G. Gibbs, S. Kothari, D. Saintillan, Y. P. Zhao, *Nano Lett.* **2011**, *11*, 2543.
- [6] S. Sanchez, M. Pumera, *Chem. Asian J.* **2009**, *4*, 1402.
- [7] Z. Wu, Y. Wu, W. He, X. Lin, J. Sun, Q. He, *Angew. Chem. Int. Ed.* **2013**, *52*, 7000.
- [8] G. Loget, A. Kuhn, *Nat. Commun.* **2011**, *2*, 535.
- [9] S. Sánchez, L. Soler, J. Katuri, *Angew. Chem. Int. Ed.* **2015**, *54*, 1414.
- [10] W. Gao, S. Sattayasamitsathit, K. M. Manesh, D. Weihs, J. Wang, *J. Am. Chem. Soc.* **2010**, *132*, 14403.
- [11] W. Gao, J. Wang, *ACS Nano* **2014**, *8*, 3170.
- [12] S. Kim, F. Qiu, S. Kim, A. Ghanbari, C. Moon, L. Zhang, B. J. Nelson, H. Choi, *Adv. Mater.* **2013**, *25*, 5863.
- [13] W. Gao, A. Uygun, J. Wang, *J. Am. Chem. Soc.* **2012**, *134*, 897.
- [14] T. Xu, F. Soto, W. Gao, V. Garcia-Gradilla, J. Li, X. Zhang, J. Wang, *J. Am. Chem. Soc.* **2014**, *136*, 8552.
- [15] J. Li, J. Zhang, W. Gao, G. Huang, Z. Di, R. Liu, J. Wang, Y. Mei, *Adv. Mater.* **2013**, *25*, 3715.
- [16] D. A. Wilson, R. J. Nolte, J. C. van Hest, *Nat. Chem.* **2012**, *4*, 268.
- [17] A. Ghosh, P. Fischer, *Nano Lett.* **2009**, *9*, 2243.
- [18] J. Wang, *ACS Nano* **2009**, *3*, 4.
- [19] S. Sanchez, A. A. Solovov, S. Schulze, O. G. Schmidt, *Chem. Commun.* **2011**, *47*, 698.
- [20] Z. Wu, X. Lin, Y. Wu, T. Si, J. Sun, Q. He, *ACS Nano* **2014**, *8*, 6097.
- [21] J. Wang, W. Gao, *ACS Nano* **2012**, *6*, 5745.
- [22] W. Gao, D. Kagan, O. S. Pak, C. Clawson, S. Campuzano, E. Chuluun-Erdene, E. Shipton, E. E. Fullerton, L. Zhang, E. Lauga, *J. Wang, Small* **2012**, *8*, 460.
- [23] S. Campuzano, J. Orozco, D. Kagan, M. Guix, W. Gao, S. Sattayasamitsathit, J. C. Claussen, A. Merkoci, J. Wang, *Nano Lett.* **2012**, *12*, 396.
- [24] C.-M. J. Hu, R. H. Fang, B. T. Luk, K. N. H. Chen, C. Carpenter, W. Gao, K. Zhang, L. Zhang, *Nanoscale* **2013**, *5*, 2664.
- [25] C.-M. J. Hu, R. H. Fang, L. Zhang, *Adv. Healthcare Mater.* **2012**, *1*, 537.
- [26] Z. Wu, T. Li, J. Li, W. Gao, T. Xu, C. Christianson, W. Gao, M. Galarnyk, Q. He, L. Zhang, J. Wang, *ACS Nano* **2014**, *8*, 12041.
- [27] C.-M. J. Hu, L. Zhang, S. Aryal, C. Cheung, R. H. Fang, L. Zhang, *Proc. Natl. Acad. Sci. U.S.A.* **2011**, *108*, 10980.
- [28] C.-M. J. Hu, R. H. Fang, J. Copp, B. Luk, L. Zhang, *Nat. Nanotechnol.* **2013**, *8*, 336.
- [29] C.-M. J. Hu, R. H. Fang, B. Luk, L. Zhang, *Nat. Nanotechnol.* **2013**, *8*, 933.
- [30] J. Copp, R. H. Fang, B. Luk, C.-M. J. Hu, W. Gao, K. Zhang, L. Zhang, *Proc. Natl. Acad. Sci. U.S.A.* **2014**, *111*, 13481.
- [31] W. Gao, C.-M. J. Hu, R. H. Fang, B. T. Luk, J. Su, L. Zhang, *Adv. Mater.* **2013**, *25*, 3549.

- [32] D. Dell'Orco, M. Lundqvist, T. Cedervall, S. Linse, *Nanomedicine* **2013**, *8*, 1271.
- [33] R. H. Fang, C.-M. J. Hu, K. N. H. Chen, B. T. Luk, C. W. Carpenter, W. Gao, S. Li, D.-E. Zhang, W. Lu, L. Zhang, *Nanoscale* **2013**, *5*, 8884.
- [34] C.-M. J. Hu, L. Zhang, *Nano Today* **2014**, *9*, 401.
- [35] J.-G. Piao, L. Wang, F. Gao, Y.-Z. You, Y. Xiong, L. Yang, *ACS Nano* **2014**, *8*, 10414.
- [36] B. T. Luk, C.-M. J. Hu, R. H. Fang, D. Dehaini, C. Carpenter, W. Gao, L. Zhang, *Nanoscale* **2014**, *6*, 2730.
- [37] V. Garcia-Gradilla, J. Orozco, S. Sattayasamitsathit, F. Soto, F. Kuralay, A. Pourazary, A. Katzenberg, W. Gao, Y. Shen, J. Wang, *ACS Nano* **2013**, *7*, 9232.
- [38] D. Pornpattananangkul, L. Zhang, S. Olson, S. Aryal, M. Obonyo, K. Vecchio, C. M. Huang, L. Zhang, *J. Am. Chem. Soc.* **2011**, *133*, 4132.
- [39] S. Thamphiwatana, V. Fu, J. Zhu, D. Lu, W. Gao, L. Zhang, *Langmuir* **2013**, *29*, 12228.
- [40] C.-M. J. Hu, R. H. Fang, B. T. Luk, L. Zhang, *Nanoscale* **2014**, *6*, 65.
- [41] W. Wang, L. A. Castro, M. Hoyos, T. E. Mallouk, *ACS Nano* **2012**, *6*, 6122.
- [42] T. Xu, F. Soto, W. Gao, R. Dong, V. Garcia-Gradilla, E. Magana, X. Zhang, J. Wang, *J. Am. Chem. Soc.* **2015**, *137*, 2163.
- [43] F. Nadal, E. Lauga, *Phys. Fluids* **2014**, *26*, 082001.
- [44] T. Laurell, F. Petersson, A. Nilsson, *Chem. Soc. Rev.* **2007**, *36*, 492.
- [45] R. H. Fang, C.-M. J. Hu, B. T. Luk, W. Gao, J. A. Copp, Y. Tai, D. E. O'Connor, L. Zhang, *Nano Lett.* **2014**, *14*, 2181.